AIAA SciTech Forum
23-27 January 2023, National Harbor, MD & Online
AIAA SCITECH 2023 Forum

10.2514/6.2023-2146

Numerical prediction of drag crisis for smooth spheres using a high-order flux reconstruction method

A. M. Akbarzadeh*, M. A. Alhawwary*, F. D. Witherden†, and A. Jameson ‡

High-fidelity simulations of flow over a smooth sphere at high Reynolds numbers ranging from 1.0×10^5 to 3.0×10^5 are performed using the high-order flux reconstruction method (FR) implemented in the massively parallel high-order solver PyFR. The main goal of this study is to numerically predict the range of drag crisis of smooth spheres and validate the results against experimental data to assess the efficiency of high-order methods for such problems. To ensure that the range for critical Reynolds number is predicted accurately, simulations are performed using 12 meshes with different computational mesh sizes and mesh types at $Re = 1.0 \times 10^5$, $Re = 2.0 \times 10^5$ and $Re = 3.0 \times 10^5$. The results show that drag crisis can be predicted numerically with an almost DNS boundary layer grid resolution and with high (p) polynomial orders. The simulations predict drag coefficients of $C_D = 0.4635$ and $C_D = 0.1292$ at $Re = 2 \times 10^5$ and $Re = 3 \times 10^5$, respectively, which confirms that $Re = 2 \times 10^5$ and $Re = 3 \times 10^5$ are in the range of subcritical and critical Reynolds number. The flow analysis shows that at subcritical Re, laminar separation occurs without reattachment, whereas at critical Re, there is laminar boundary layer separation, turbulent boundary layer reattachment and turbulent boundary layer separation.

I. Introduction

Drag crisis is a well-known phenomenon in fluid dynamics that is characterized by a drop in drag coefficient of bluff bodies, e.g., cylinder and sphere, due to boundary layer transition to turbulence. During the drag crisis, the mean drag coefficient of a sphere decreases from about 0.5 to its minimum, which is around 0.1 [1]. Based on the drag coefficient, the flow over sphere is classified into four regimes [1]: (I) sub-critical at which the drag coefficient is around 0.5 and boundary layer is laminar ($Re < 10^5$), (II) critical regime where the boundary layer transition and drag crisis occurs, which is our interested regime, (III) super-critical where drag remains almost constant around 0.1, and (IV) transcritical regime ($Re > 5 \times 10^5$) in which the boundary layer transition point moves towards upstream and drag increases. Although the critical drag force has been measured experimentally by many researchers, the literature concerning the drag crisis is sparse. For example, the critical Reynolds number, i.e., the Reynolds number at which the drag crisis starts, ranges from 1.2×10^5 to 4×10^5. [1–4]. The reason for this discrepancy is the high sensitivity of the flow to the surface roughness and experimental setup. It has been observed that the flow is greatly affected by surface roughness, free stream turbulence, tunnel blockage, and method of support[2, 5]. For example a surface roughness of $k/D \approx 10^{-5}$ or an isolated roughness can significantly reduce the critical Reynolds number [2, 6]. On the other hand, the numerical prediction is exacting due to the resolution requirements imposed by a very thin (possibly transitioning) boundary layer and a broad wake combined with the low-frequency content. Consequently, most of previous numerical studies focused on subcritical or super-critical regimes [7, 8] and there is a lack of numerical studies on predicting the drag crisis. Nevertheless, due to the recent development of high-order methods and improvement of computational resources using modern GPUs, the numerical prediction of the drag crisis might be feasible. It is in this context that we aim to address this issue by employing high-fidelity simulations based on high-order discretization methods.

In this study, the open-source software PyFR [9] for high-order massively parallel computations is employed to simulate the unsteady turbulent flow over a smooth sphere at high Reynolds numbers, ranging from 300K> Re >100K to accurately predict the drag crisis. This manuscript is organized as follows. In §II the governing equations and numerical method for solving the flow equations are illustrated briefly. The simulation and case setup are presented in §III, and the results are presented in §IV.

*Postdoctoral Researcher, Department of Aerospace engineering, Texas A&M University, College Station, TX
†Assistant Professor, Department of Ocean engineering, Texas A&M University, College Station, TX
‡Professor, Department of Aerospace engineering, Texas A&M University, College Station, TX

II. Methodology

In this study, we use PyFR, in which the compressible Navier–Stokes equations are solved with a multidimensional Flux reconstruction (FR) approach. PyFR is an open-source software that can solve the compressible Navier–Stokes equations on mixed unstructured grids and is designed to target a range of modern hardware platforms, including heterogeneous mixtures of CPUs and GPUs, via C/OpenMP, CUDA, HIP, and OpenCL backends [9, 10]. The FR approach introduced by Huynh [11] is a nodal numerical formulations for solving hyperbolic partial differential equations. The method has been further developed by several groups [12–14] for advection-diffusion problems and extended to mixed unstructured grids [10, 15]. In addition, high-order FR method has proved successful for a number of large eddy simulations based on the implicit approach [16] as shown in [17–20] and more recently based on the Partially Averaged Navier-Stokes equations (PANS) in Dzanic et. al [21]. Interested readers about the FR method can consult the following reviews [22, 23].

Here, we briefly present the FR method. Navier-Stokes equations can be written in a conservative form as follows,

$$\frac{\partial \mathbf{u}}{\partial t} + \boldsymbol{\nabla} \cdot \mathbf{f} = 0, \tag{1}$$

where $\mathbf{u} = \mathbf{u}(\mathbf{x}, t)$= $(\rho, \rho v_x, \rho v_y, \rho v_z, E)$, is the solution, ρ is the density, $\mathbf{v} = (v_x, v_y, v_z)$ are the fluid velocity components in x, y, z directions, respectively, and E is the total energy per volume of the fluid. Here, $\mathbf{f} = \mathbf{f}(\mathbf{u}, \boldsymbol{\nabla}\mathbf{u}) = \mathbf{f}^i - \mathbf{f}^v$ is the flux with $\mathbf{f}^i$ the inviscid flux given by

$$\mathbf{f}^i = \begin{pmatrix} \rho v_x & \rho v_y & \rho v_z \\ \rho {v_x}^2 + p & \rho v_x v_y & \rho v_x v_z \\ \rho v_x v_y & \rho {v_y}^2 + p & \rho v_y v_z \\ \rho v_x v_z & \rho v_y v_z & \rho {v_z}^2 + p \\ v_x(E+p) & v_x(E+p) & v_z(E+p) \end{pmatrix}, \tag{2}$$

where p is the pressure which is for an ideal gas is

$$p = (\gamma - 1)(E - \frac{1}{2}\rho ||\mathbf{v}||^2), \tag{3}$$

where $\gamma = c_p/c_v$, where c_p and c_v are specific heat capacities at constant pressure and volume, respectively. The viscous flux ($\mathbf{f}^\mathbf{v}$) is

$$\mathbf{f}^v = \begin{pmatrix} 0 & 0 & 0 \\ \tau_{xx} & \tau_{yx} & \tau_{zx} \\ \tau_{xy} & \tau_{yy} & \tau_{zy} \\ \tau_{xz} & \tau_{yz} & \tau_{zz} \\ v_i\tau_{ix} + \Delta\partial_x T & v_i\tau_{iy} + \Delta\partial_y T & v_i\tau_{iz} + \Delta\partial_z T \end{pmatrix}. \tag{4}$$

In the above we have defined $\Delta = \mu c_p/Pr$ where μ is the dynamic viscosity and Pr is the Prandtl number. The components of the stress–energy tensor are given by

$$\tau_{ij} = \mu(\partial_i v_j + \partial_j v_i) - \frac{2}{3}\mu\delta_{ij}\boldsymbol{\nabla} \cdot \mathbf{v}. \tag{5}$$

Using the ideal gas law, the temperature is

$$T = \frac{1}{c_v}\frac{1}{\gamma - 1}\frac{p}{\rho}. \tag{6}$$

In the current study, values of $\gamma = 1.4$ and $Pr = 0.71$, and flow Mach number is $M = 0.1$ were employed.

PyFR is based on the high-order flux reconstruction approach of Huynh [11]. In the present work, third-order polynomials were used to represent the solution within each element of the mesh, thus nominally achieving fourth-order accuracy in space. A Rusanov Riemann solver was used to calculate the interelement inviscid fluxes, the local discontinuous Galerkin [24] approach was used to calculate the inter-element viscous fluxes, an adaptive time-step Runge-Kutta (RK45) scheme [25] was utilized to advance the solution in time.

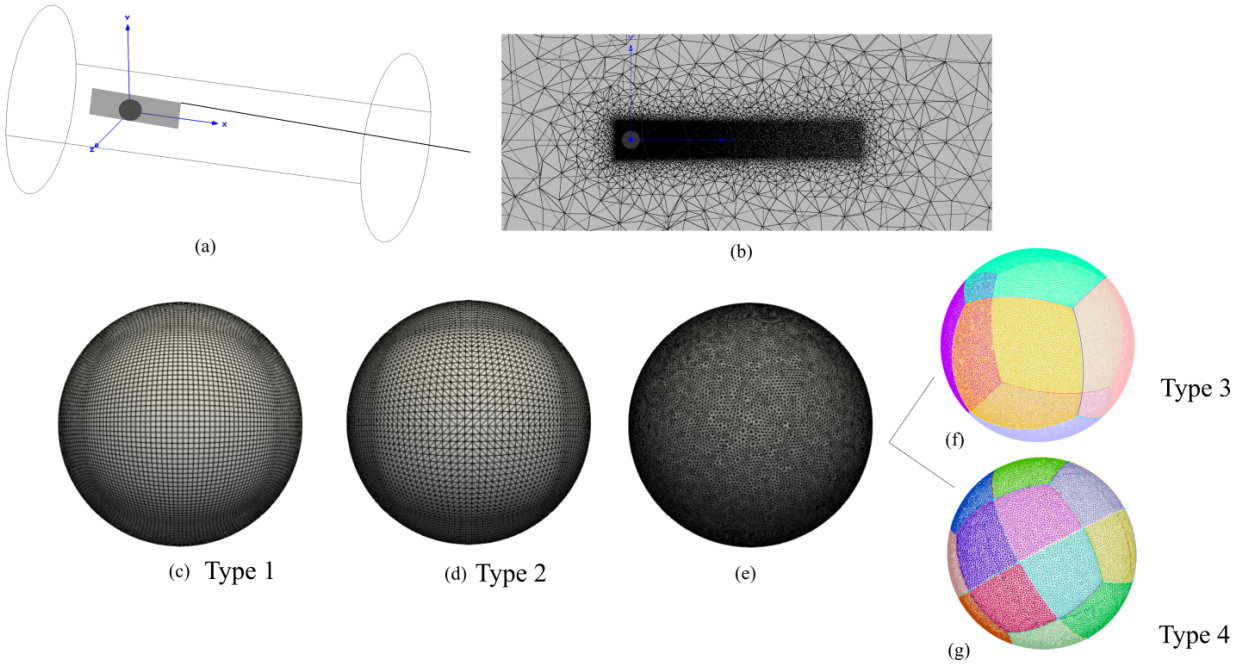

Fig. 1 Computational domain, and different sphere surface mesh types: c) type 1: quad surface mesh, d) type 2: diagonalized triangles, f) type 3: 6 domain delaunay triangle, and g) 24 domain delaunay triangle.

III. Setup

In this section the simulation setup is explained. The simulation setup is presented in Fig. 1. There are four types of surface mesh and two types of domains generated for the grid sensitivity study. First mesh type is composed of only hex meshes. In this mesh, the sphere surface is meshed with quadrilaterals that has been extruded along the normal direction with 41 elements which resulted in a O-O type grid with diameter of about $52D$ (Fig. 1c). The rest of meshes are unstructured meshes with a cylindrical domain of radius of 25D and length of 100D. The sphere is located at 25D of the inflow (Fig. 1a) and the wake the sphere is refined up to $L = 10D$ with tetrahedral mesh (Fig. 1b). The surface mesh is triangular surface mesh (Fig. 1d, e). Three types of triangular surface mesh are generated i) diagonalized triangles (Fig. 1d), ii) 6-zones delaunay triangles (Fig. 1f), and iii) 24 zones triangles (Fig. 1g). The boundary layer mesh is prism which has been generated by extruding the surface cells along the radius for at least 11 layers.

It should be noted that all mesh are curved and generated with Pointwise. For each mesh types, multiple grids with different mesh sizes are generated, which are reported in Table 1. Here, the first element's height ranges from $0.0007D$ to $0.002D$ (Table 1). Among these meshes, mesh 10 has the highest grid resolution, with ~9.75 million prisms and ~9.7 million tetrahedra for a total of ~19.45 millions elements. This corresponds to ~583 million degrees of freedom (DOF) per equation.

The numerical y^+ is plotted for mesh 10 at $Re = 3 \times 10^5$, based on the closest p-3 solution point to the wall at conventional time $t = 71U/D$ in Fig. 2. The contour of instantaneous y^+ shows that the the maximum y^+ of the first solution point is less than 1.3. Figure 2b presents the plot of the averaged y^+ along azimuthal angle. It can be seen that mean y^+ is less than 0.6. Moreover, the maximum edge length l_c along the circumference of the sphere ranges between $0.001258D$ to $0.004754D$, which corresponds to a maximum element aspect ratio of $l_c/h < 6.7$ on the sphere.

The simulations are initiated from a freestream initial condition ($u_x = 1$, $u_y = 0$, $u_z = 0$), with $\rho = 1$ and Mach number=$M = U/c = 0.1$ resulting in the nondimensional atmospheric pressure of $p = 71.4285$. Riemann-invariant boundary conditions are applied on the farfield and no-slip adiabatic boundary condition is applied on the surface of the sphere. All of the simulations started with a first-order polynomials (second-order accuracy) for at least 60 convective time (D/U), afterwards, they are restarted for at least $35D/U$ with a third-order polynomials and the averaged data is obtained from the final $20D/U$. Here, mesh 10 has the highest grid resolution. Thus, the results are discussed based on this mesh.

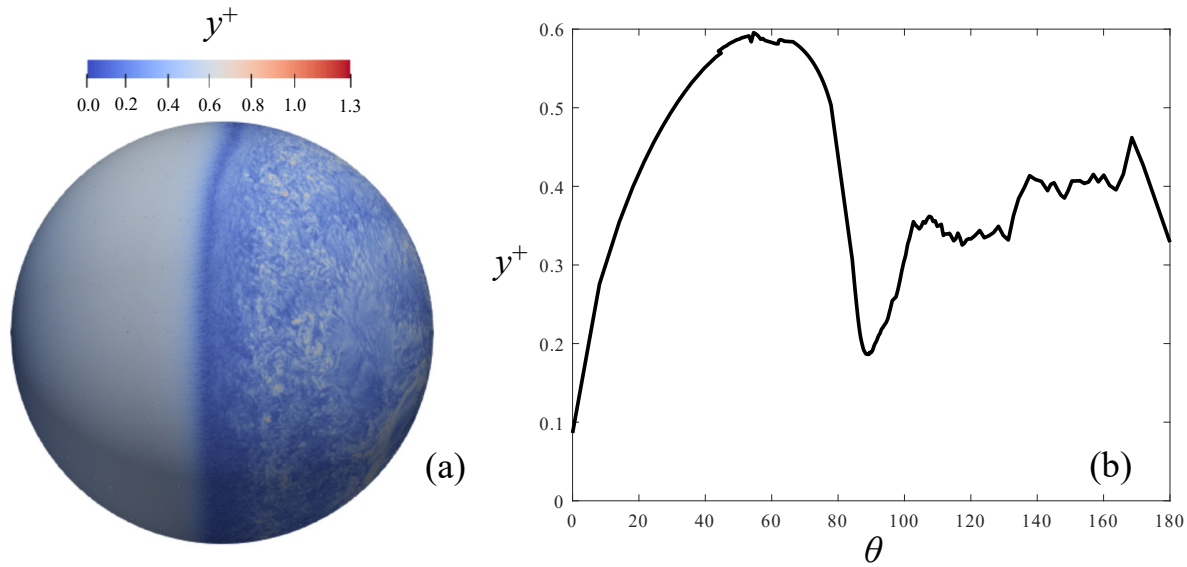

Fig. 2 Numerical y^+ of mesh 10 at $Re = 3 \times 10^5$ based on instantaneous flow at $t = 71U/D$. (a): contours of instantaneous y^+, (b): profile of averaged y^+ along constant azimuthal angle (θ)

IV. Results and discussion

In this section the results of the simulations are presented. In §IV.A mean force coefficients are plotted against the experimental data. Later, in §IV.B, the instantaneous flow field and turbulence statistics are presented.

A. Force coefficients

The drag coefficient for three Reynolds number: $Re = 1.0\times10^5$, $Re = 2.0\times10^5$, and $Re = 3.0\times10^5$ ($C_D = \frac{4F_D}{0.5\rho U^2 \pi D^2}$, F_D: the drag force) based on p3 simulation is plotted in Fig. 3 and compared against the previous experiments of Norman and McKeon [3], Achenbach [1], Wieselsberger [4], and Deshanpe et al. [26]. The C_D plot shows a great discrepancy in both experiments and numerical results, in particular at $Re \geq 2.0 \times 10^5$. The classical experiments of Achenbach [1] predicts that the Reynolds number for the critical regime is approximately $3.3 \times 10^5 \leq Re \leq 4.4 \times 10^5$ while the experiment of Norman and McKeon [3] reports the critical Re as $2.6 \times 10^5 \leq Re \leq 3.5 \times 10^5$. At However, all experiments agree well at the subcritical range $Re < 2 \times 10^5$. Similarly, the results of simulations are grid insensitive at $Re = 10^5$, e.g., C_D ranges from 0.4952 to 0.5124 which is in the range of values reported in the literature [1, 3]. Nevertheless, at $Re = 2.0 \times 10^5$, the drag force prediction becomes grid dependent when the surface mesh is not sufficiently resolved. For example, comparing the drag force of meshes 7 and 8 reveals that C_D can change significantly by only increasing the number of surface cells. The C_D of fine meshes (9 and 10) are almost similar at $Re = 2.0 \times 10^5$ and they are in good agreement with the experimental measurements [3, 26]. Nevertheless, there is about 22.3% discrepancy at $Re = 3 \times 10^5$ comparing drag of mesh 9 and 10. Here, at $Re = 3 \times 10^5$, flow is in the critical regime (Fig. 3), similar to the experiment of Norman and McKeon [3].

To present the force coefficients quantitatively and see the effect of high-order polynomial calculations, the value of C_D, σ_{C_D}, C_y, and C_z are presented in Table 2 for both p1 and p3 simulations. Here, σ_{C_D} is the standard deviation of C_D, C_y and C_Z are force coefficients along y and z axis, respectively. There is about 5.6% discrepancy in the drag coefficient at $Re = 2.0 \times 10^5$ of mesh 9 and 10. At $Re = 3.0 \times 10^5$, the C_D varies by 22.4% for p3 simulations since C_D is in the critical range. The side forces C_y and C_z are nonzero which is probably due to insufficient averaging. The non-zero force coefficient along circumferential directions is reported in the previous studies [3, 7].

The sudden drag drop at $Re = 3.0 \times 10^5$ is due to a delay in boundary layer separation, where the separation point can be quantified by the skin friction coefficient $C_f = \frac{\tau_w}{\rho U^2}\sqrt{Re}$, i.e., $c_f < 0$. Figure 4 presents the time-averaged skin friction (C_f) and pressure coefficient ($C_p = \frac{p-p_\infty}{0.5\rho U^2}$) averaged along a constant azimuthal angle ($0 \leq \theta \leq 180$) for both p1 and p3 simulations with the finest mesh (mesh 10). The zero C_f represent the separation point and the negative C_f shows the recirculation zone. The profile of C_f (Fig. 4) shows that at $Re = 2 \times 10^5$, the flow becomes separated at

Table 1 Mesh names, types and sizes. Number of surface cells refers to the number of quadrilateral or triangles on the surface of the sphere.

Mesh number	Mesh type	Number of surface cells	Wall normal spacing
1	Type 1	15000	0.002D
2	Type 1	60000	0.002D
3	Type 2	14700	0.002D
4	Type 2	120000	0.001D
5	Type 3	24622	0.002D
6	Type 3	50254	0.002D
7	Type 3	50254	0.001D
8	Type 3	204154	0.001D
9	Type 3	458769	0.0008D
10	Type 3	810166	0.0007D
11	Type 4	51245	0.001D
12	Type 4	203568	0.001D

$\theta = 86.2^o$ and does not reattach as C_f remains negative. Comparaing p1 and p3 simulations, it can be observed that C_f plot of p1 simulation has small discrepancy near the separation points, e.g., separation point is 91.2. The separation can also be observed in the C_p profile. A plateau is generated at the separation zone. It can also be observed that the C_p profile is in good agreement with the experiment of Achenbach at $Re = 1.6 \times 10^5$ although Re is not identical to the present study. At the critical Reynolds number, $Re = 3 \times 10^5$, the separation point moves towards downstream, i.e., $\theta = 103.4^o$ (for p3 simulation). After the separation, the separated shear layer becomes turbulent and reattaches due the enhanced momentum and creates a turbulent boundary layer. The generation of the turbulent boundary layer can be observed by the sharp enhancement in the C_f at $\theta = 119^o$. The attached boundary layer, later, separates at $\theta = 143^o$. Comparing the p1 and p3 results, a high discrepancy can be observed near the separated zone $\theta > 102.0$. The laminar separation and turbulent reattachment has been reported in the experiment of Deshpande et al. [26] at $Re = 3.72 \times 10^5$ though they observed the critical Re ranging from 3.4×10^5 to 4.4×10^5 (see Fig. 3). At crtitcal regime, $Re = 3 \times 10^5$, the C_p profile is similar to the experiment of Deshanpe et al. at $Re = 3.72 \times 10^5$, however, it has a discrepancy with Achenbach experiment at $Re = 3.1 \times 10^5$ high azimuthal angle $\theta > 90^o$ because the boundary layer was laminar at $Re = 3.1 \times 10^5$ [1].

Table 2 Force coefficients.

Mesh number	p-order	Re	C_D	σ_{C_D}	C_y	C_z
8	p3	1.0×10^5	0.5124	0.0552	-0.0086	0.0093
9	p1	2.0×10^5	0.4813	0.03054	0.0015	0.022
9	p3	2.0×10^5	0.4787	0.0449	0.0009	0.0052
10	p1	2.0×10^5	0.5013	0.0296	-0.0137	0.0183
10	p3	2.0×10^5	0.4635	0.0417	0.0052	0.0103
9	p1	3.0×10^5	0.1129	0.019	0.0132	-0.0014
9	p3	3.0×10^5	0.0940	0.0210	-0.0086	0.0009
10	p1	3.0×10^5	0.1145	0.0354	0.0243	0.0156
10	p3	3.0×10^5	0.1272	0.0206	0.0023	-0.0017

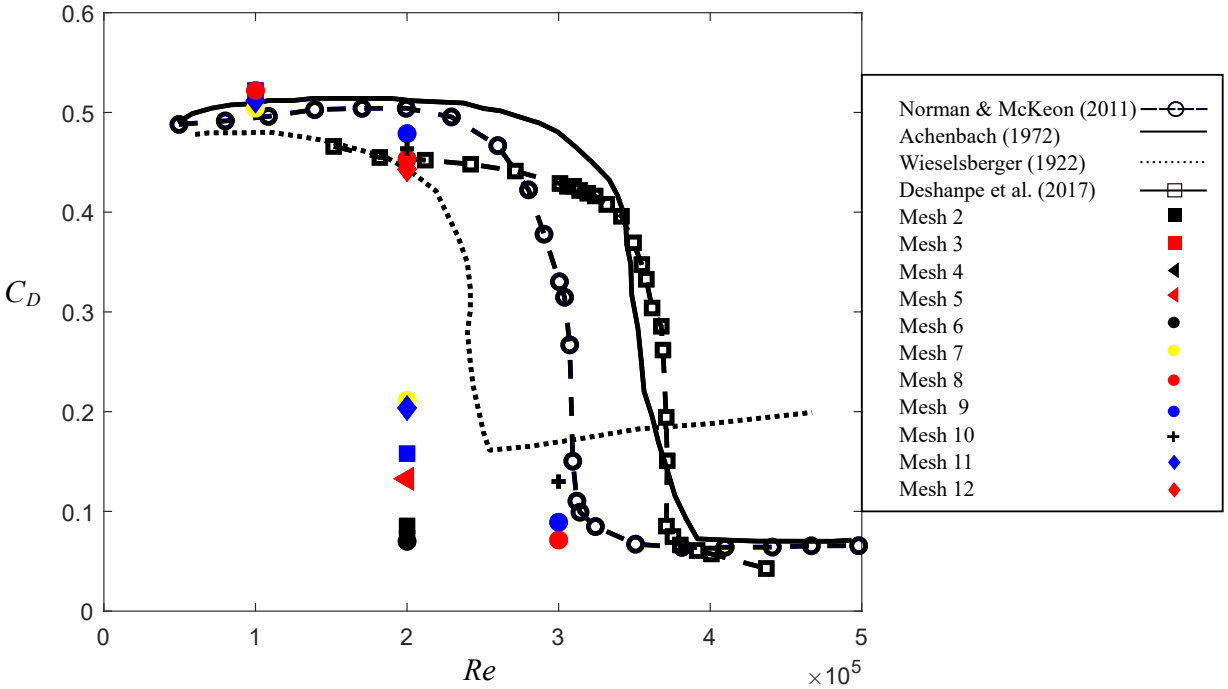

Fig. 3 Drag coefficient against Reynolds number for different meshes.

B. Flow visualization

The instantaneous wake of the sphere is presented for two Re by the contours of out-of-plane vorticity in Fig. 5 for mesh 10. It can be observed that by increasing the Reynolds number the sphere wake becomes smaller as the flow separation point moves towards the downstream. The thin boundary layer separates and creates a turbulent wake. However, at $Re = 3 \times 10^5$, the separation is delayed and separation zone is smaller compared to the lower Re case due to the further turbulent reattachment.

The sphere wake is also presented by the contours of streamwise velocity at two planes along the streamwise direction, i.e., $x = 0.3$ and $x = 0.4$ from the center of the sphere, in Fig. 6. Comparing the wake of the sphere at different Re shows greater reverse flow at critical Re, which agrees with the vorticity visualization in Fig. 5. Furthermore, at $x = 0.4$, the turbulent wake is clearly visible for both cases. However, at $x = 0.4$, a turbulent wake is generated for the sub-critical Re case due to the flow separation at upstream, but there is no reverse flow at higher Re case.

V. Conclusions and Future work

The Critical Reynolds number of a smooth sphere is numerically predicted using the high-order flux reconstruction method (FR). Simulations are performed at three Reynolds number, $Re = 10^5$, $Re = 2 \times 10^5$ and $Re = 3 \times 10^5$. The simulations predict drag coefficients of $C_D = 0.4635$ and $C_D = 0.0948$ at $Re = 2 \times 10^5$ and $Re = 3 \times 10^5$, respectively, which demonstrates that $Re = 2 \times 10^5$ and $Re = 3 \times 10^5$ are in the range of subcritical and critical Reynolds number, respectively. The predicted range is in good agreement with Norman and McKeon experiments [3] and the pressure coefficient profile at critical Reynolds number agrees well with the experiment of Deshanpe [**?**]. The similarity of drag coefficient and profile of the pressure coefficient with these experiments shows the capability of high-order methods for accurate prediction of turbulence transition for complex geometries at high Reynolds numbers. The flow analysis shows that at subcritical Re, laminar separation occurs without a reattachment, whereas at critical Re, the laminar boundary layer separates, reattaches further downstream and create a turbulent boundary layer. Nevertheless, understanding the turbulent transition mechanism of flow over smooth sphere requires further analysis which is a part of the future work. In addition, more simulations are required at $Re > 3 \times 10^5$ and $2 \times 10^5 < Re < 3 \times 10^5$ to estimate the C_D profile against Re.

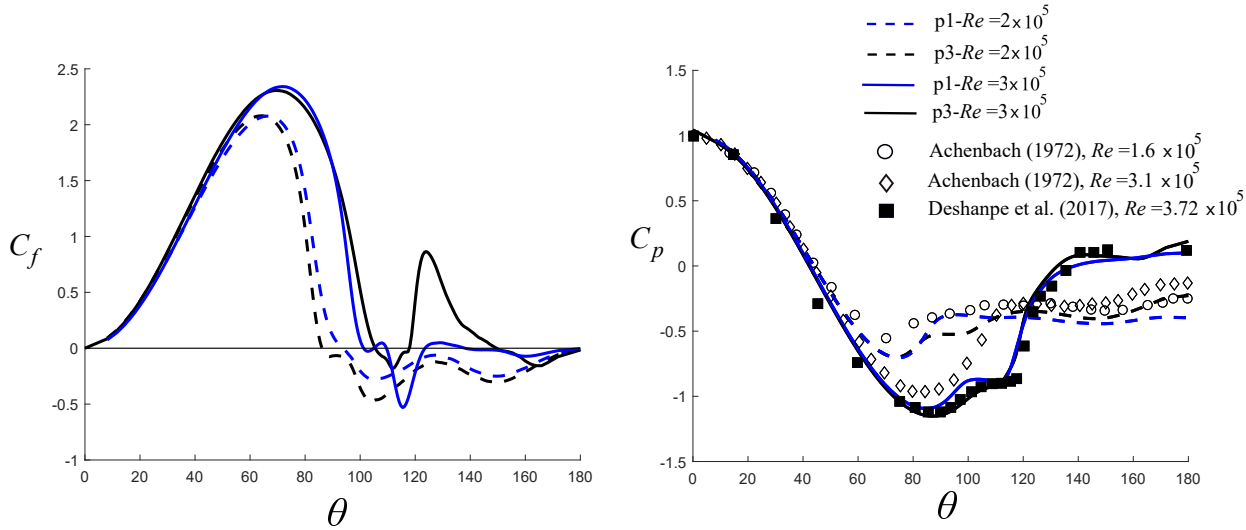

Fig. 4 profile of pressure coefficient, $C_p = \frac{p-p_\infty}{0.5\rho U^2}$ and normalized skin friction, $C_f = \frac{\tau_w}{\rho U^2}\sqrt{Re}$.

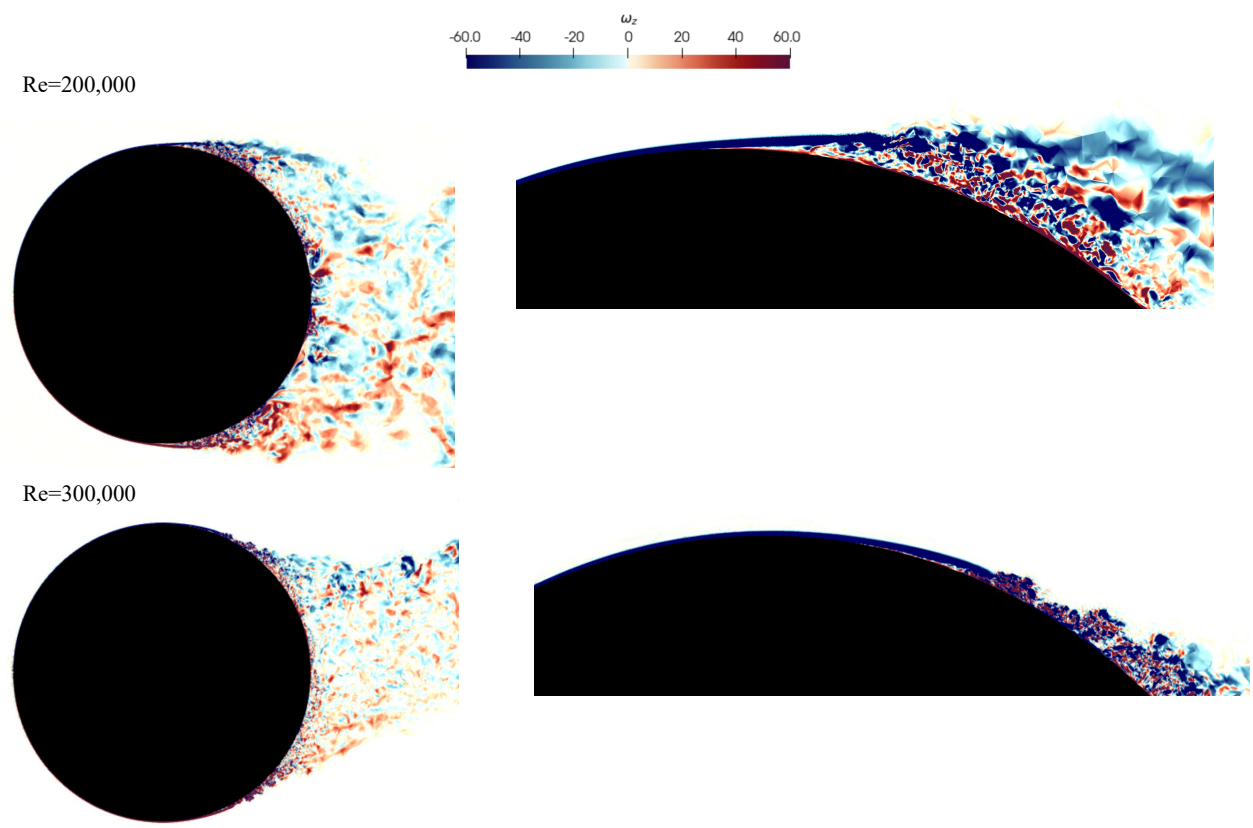

Fig. 5 Contours of out-of-plane vorticity in the wake of the sphere at t = 74.001.

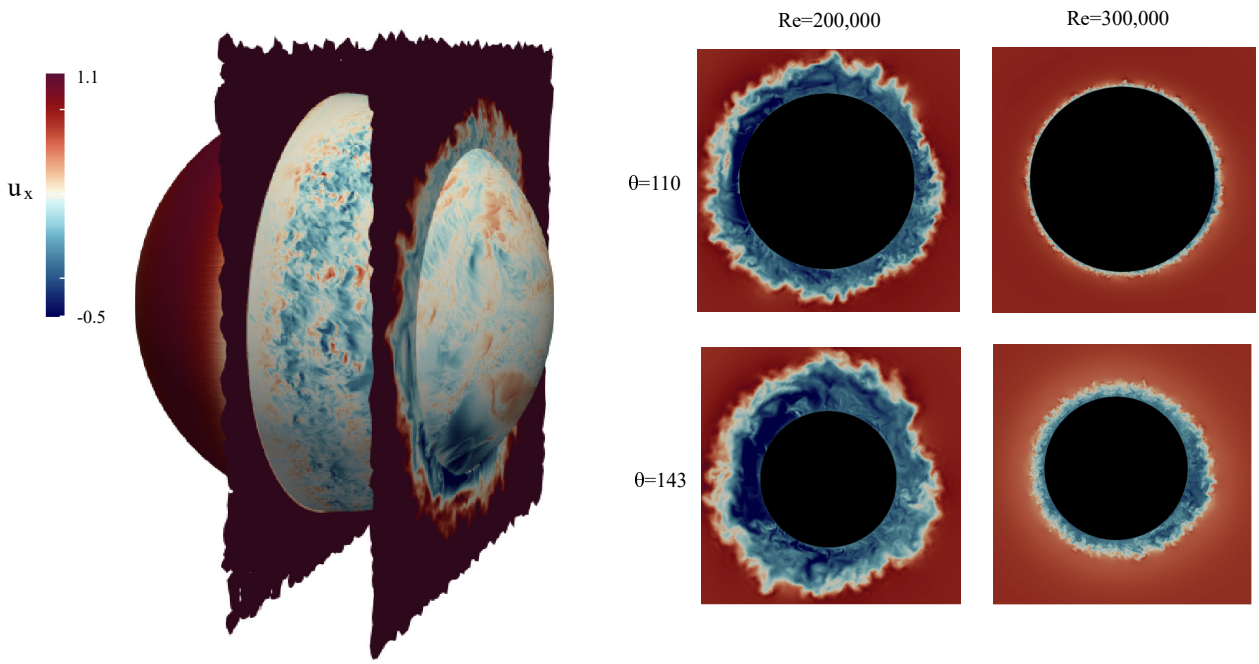

Fig. 6 Contours of streamwise velocity at different steamwise sections at $t = 74.001$.

References

[1] Achenbach, E., "Experiments on the flow past spheres at very high Reynolds numbers," *Journal of Fluid Mechanics*, Vol. 54, No. 3, 1972, pp. 565–575. https://doi.org/10.1017/s0022112072000874.

[2] Achenbach, E., "The effects of surface roughness and tunnel blockage on the flow past spheres," *Journal of Fluid Mechanics*, Vol. 65, No. 1, 1974, p. 113–125. https://doi.org/10.1017/S0022112074001285.

[3] Norman, A. K., and McKeon, B. J., "Unsteady force measurements in sphere flow from subcritical to supercritical Reynolds numbers," *Experiments in Fluids*, Vol. 51, No. 5, 2011, pp. 1439–1453. https://doi.org/10.1007/s00348-011-1161-8.

[4] Wieselsberger, C. v., "Neuere feststellungen uber die gesetze des flussigkeits und luftwiderstands," *Phys. Z.*, Vol. 22, 1921, p. 321.

[5] Bacon, D. L., and Reid, E. G., "The resistance of spheres in wind tunnels and in air," Tech. rep., 1924.

[6] Norman, A. K., and McKeon, B. J., "The effect of a small isolated roughness element on the forces on a sphere in uniform flow," *Experiments in Fluids*, Vol. 51, No. 4, 2011, pp. 1031–1045. https://doi.org/10.1007/s00348-011-1126-y.

[7] Constantinescu, G., and Squires, K., "Numerical investigations of flow over a sphere in the subcritical and supercritical regimes," *Physics of Fluids*, Vol. 16, No. 5, 2004, pp. 1449–1466. https://doi.org/10.1063/1.1688325.

[8] RODRIGUEZ, I., BORELL, R., LEHMKUHL, O., SEGARRA, C. D. P., and OLIVA, A., "Direct numerical simulation of the flow over a sphere at $Re = 3700$," *Journal of Fluid Mechanics*, Vol. 679, 2011, pp. 263–287. https://doi.org/10.1017/jfm.2011.136.

[9] Witherden, F., Farrington, A., and Vincent, P., "PyFR: An open source framework for solving advection–diffusion type problems on streaming architectures using the flux reconstruction approach," *Computer Physics Communications*, Vol. 185, No. 11, 2014, pp. 3028–3040. https://doi.org/10.1016/j.cpc.2014.07.011.

[10] Witherden, F., Vermeire, B., and Vincent, P., "Heterogeneous computing on mixed unstructured grids with PyFR," *Computers & Fluids*, Vol. 120, 2015, pp. 173–186. https://doi.org/10.1016/j.compfluid.2015.07.016.

[11] Huynh, H. T., "A Flux Reconstruction Approach to High-Order Schemes Including Discontinuous Galerkin Methods," *18th AIAA Computational Fluid Dynamics Conference*, American Institute of Aeronautics and Astronautics, 2007. https://doi.org/10.2514/6.2007-4079.

[12] Vincent, P. E., Castonguay, P., and Jameson, A., "A New Class of High-Order Energy Stable Flux Reconstruction Schemes," *J. Sci. Comput.*, Vol. 47, No. 1, 2011, pp. 50–72. https://doi.org/10.1007/s10915-010-9420-z.

[13] Castonguay, P., Williams, D. M., Vincent, P. E., and Jameson, A., "Energy Stable Flux Reconstruction Schemes for Advection–Diffusion Problems," *Comput. Methods Appl. Mech. Eng.*, Vol. 267, 2013, pp. 400–417. https://doi.org/10.1016/j.cma.2013.08.012.

[14] Gao, H., Wang, Z. J., and Huynh, H. T., "Differential Formulation of Discontinuous Galerkin and Related Methods for the Navier-Stokes Equations," *Commun. Comput. Phys.*, Vol. 13, No. 04, 2013, pp. 1013–1044. https://doi.org/10.4208/cicp.020611.090312a.

[15] Wang, Z., and Gao, H., "A unifying lifting collocation penalty formulation including the discontinuous Galerkin, spectral volume/difference methods for conservation laws on mixed grids," *Journal of Computational Physics*, Vol. 228, No. 21, 2009, pp. 8161–8186. https://doi.org/https://doi.org/10.1016/j.jcp.2009.07.036.

[16] Vermeire, B., and Vincent, P., "On the Properties of Energy Stable Flux Reconstruction Schemes for Implicit Large Eddy Simulation," *J. Comput. Phys.*, Vol. 327, 2016, pp. 368–388. https://doi.org/10.1016/j.jcp.2016.09.034.

[17] Wang, Z. J., Li, Y., Jia, F., Laskowski, G. M., Kopriva, J., Paliath, U., and Bhaskaran, R., "Towards Industrial Large Eddy Simulation Using the FR/CPR Method," *Comput. Fluids*, Vol. 156, 2017, pp. 579–589. https://doi.org/10.1016/j.compfluid.2017.04.026.

[18] Crabill, J., Witherden, F., and Jameson, A., "A parallel direct cut algorithm for high-order overset methods with application to a spinning golf ball," *Journal of Computational Physics*, Vol. 374, 2018, pp. 692–723. https://doi.org/https://doi.org/10.1016/j.jcp.2018.05.036.

[19] Alhawwary, M. A., and Wang, Z. J., "DNS and LES of the flow over the T106C turbine using the high-order FR/CPR method," *AIAA Scitech 2020 Forum*, American Institute of Aeronautics and Astronautics, AIAA-2020-1572, 2020. https://doi.org/10.2514/6.2020-1572.

[20] Iyer, A., Abe, Y., Vermeire, B., Bechlars, P., Baier, R., Jameson, A., Witherden, F., and Vincent, P., "High-order accurate direct numerical simulation of flow over a MTU-T161 low pressure turbine blade," *Computers & Fluids*, Vol. 226, 2021, p. 104989. https://doi.org/https://doi.org/10.1016/j.compfluid.2021.104989.

[21] Dzanic, T., Girimaji, S., and Witherden, F., "Partially-averaged Navier–Stokes simulations of turbulence within a high-order flux reconstruction framework," *Journal of Computational Physics*, Vol. 456, 2022, p. 110992. https://doi.org/https://doi.org/10.1016/j.jcp.2022.110992.

[22] Huynh, H. T., Wang, Z. J., and Vincent, P. E., "High-Order Methods for Computational Fluid Dynamics: A Brief Review of Compact Differential Formulations on Unstructured Grids," *Comput. Fluids*, Vol. 98, 2014, pp. 209–220. https://doi.org/10.1016/j.compfluid.2013.12.007.

[23] Witherden, F., Vincent, P., and Jameson, A., "High-Order Flux Reconstruction Schemes," *Handbook of Numerical Analysis*, Vol. 17, Elsevier, 2016, pp. 227–263. https://doi.org/10.1016/bs.hna.2016.09.010.

[24] Cockburn, B., and Shu, C.-W., "The Local Discontinuous Galerkin Method for Time-Dependent Convection-Diffusion Systems," *SIAM J. Numer. Anal.*, Vol. 35, No. 6, 1998, pp. 2440–2463.

[25] Kennedy, C. A., Carpenter, M. H., and Lewis, R., "Low-storage, explicit Runge–Kutta schemes for the compressible Navier–Stokes equations," *Applied Numerical Mathematics*, Vol. 35, No. 3, 2000, pp. 177–219. https://doi.org/10.1016/s0168-9274(99)00141-5.

[26] Deshpande, R., Kanti, V., Desai, A., and Mittal, S., "Intermittency of laminar separation bubble on a sphere during drag crisis," *Journal of Fluid Mechanics*, Vol. 812, 2017, pp. 815–840.